



Theoretical optical spectroscopy of complex systems



A. Mosca Conte^{a,*}, C. Violante^a, M. Missori^b, F. Bechstedt^c, L. Teodonio^{a,d},
E. Ippoliti^e, P. Carloni^e, L. Guidoni^f, O. Pulci^a

^a MIFP, NAST, ETSF, CNR INFM-SMC, Università di Roma Tor Vergata, Via della Ricerca Scientifica 1, Roma, Italy

^b Istituto dei Sistemi Complessi, Consiglio Nazionale delle Ricerche, Via Salaria Km 29.300, 00016 Monterotondo Scalo (Rome), Italy

^c Institut für Festkörpertheorie und -optik, Friedrich-Schiller-Universität, Max-Wien-Platz 1, 07743 Jena, Germany

^d Istituto centrale per il restauro e la conservazione del patrimonio archivistico e librario (IC-RCPAL), Italian Minister for Cultural Heritage, Via Milano 76, 00184 Rome, Italy

^e German Research School for Simulation Sciences, Jülich, Germany

^f Università degli Studi di L'Aquila, Dipartimento di Chimica e Materiali, Via Campo di Pile, 67100 L'Aquila, Italy

ARTICLE INFO

Article history:

Available online 4 March 2013

Keywords:

Theoretical spectroscopy

Ab initio calculations

Optical properties

Density Functional Theory

Many body

ABSTRACT

We review here some of the most reliable and efficient computational theoretical ab initio techniques for the prediction of optical and electronic spectroscopic properties and show some important applications to molecules, surfaces, and solids. We investigate the role of the solvent in the optical absorption spectrum of indole molecule. We study the excited-state properties of a photo-active minimal model molecule for the retinal of rhodopsin, responsible for vision mechanism in animals. We then show a study about spectroscopic properties of Si(1 1 1) surface. Finally we simulate a bulk system: paper, that is mainly made of cellulose, a pseudo-crystalline material representing 40% of annual biomass production in the Earth.

© 2013 Elsevier B.V. All rights reserved.

1. Introduction

Ab initio computational simulations have contributed, in the last two decades, in understanding the physical behavior of molecules and solids, as witnessed by the extensive number of publications. The importance of these investigation methods was also rewarded by the scientific community by assigning the Nobel prize to Kohn in 1998, for the Density Functional Theory [1], one of the most used approach in theoretical condensed matter simulations. First principles, parameter-free simulations have reached by now a high degree of predictivity. Another great advantage of ab initio theoretical simulations with respect to phenomenological approaches is the possibility to investigate systems that have not been yet realized [2,3], or whose properties are not measurable in some particular conditions, or that are simply not experimentally achievable, but that can give important information about physical properties of real systems.

* Corresponding author. Tel.: +39 0672594741.

E-mail addresses: adriano.mosca.conte@roma2.infn.it, adrianomoscaconte@gmail.com (A.M. Conte), claudia.violante@roma2.infn.it (C. Violante), mauro.missori@isc.cnr.it (M. Missori), bech@ifto.physik.uni-jena.de (F. Bechstedt), leonardo.guidoni@univaq.it (L. Guidoni), olivia.pulci@roma2.infn.it (O. Pulci).

In the first section we briefly review some of the most modern techniques for the calculation of optical and excited-state properties. These techniques are based on quantum mechanics, and their high computational cost reduces their range of application to small systems of few hundred atoms. In this same section we show that this range of application can be extended to systems with hundred of thousand of atoms by a Quantum Mechanics/Molecular Mechanics (QM/MM) approach. In the second section we show a simple application to an indole molecule in water solution where the solvent is simulated with more than 1300 water molecules. Here we show all the potentialities of QM/MM approaches that enable to apply sophisticated methods based on Many-Body Perturbation Theory (MBPT) to this large system, and to understand the causes of the solvent shift of indole optical absorption spectrum. In the third section we investigate a photo-active molecule, the *tZt-penta-3,5-dieniminium* cation ($C_5H_6NH_2^+$), that is the Protonated Schiff Base Minimal Model (PSBMM) of the retinal of the rhodopsin. Beside its biological interest, our calculations allow to relate its optical properties to its geometry, with interesting possible applications to photovoltaic organic cells. In the fourth section we calculate electronic and optical properties of one of the most studied surfaces: the Si(1 1 1) 2×1 surface. Some aspects of its reconstruction are still debated and we give a contribution to this discussion with theoretical calculation of its electronic and optical properties for the two known isomers. In the last section, finally, we study a bulk system: paper. In particular we investigate the role of oxidation in

paper induced by aging. This is an example of how the combination of experimental and theoretical spectroscopic techniques can give information on optical, structural, and chemical properties of a complex system such as paper, and how the results provided by these combination can go beyond their pure scientific interest, and could be of interest also for the preservation of our cultural heritage.

2. Methods

Most of condensed matter simulations are performed within the Born–Oppenheimer approximation, where the total Hamiltonian is separated in an Hamiltonian for the nuclei, and one for the electrons. Ions contribution appears also in the electron Hamiltonian H through the ion–electron Coulomb interaction V_{ext} :

$$H = \sum_i -\frac{1}{2} \nabla_{\mathbf{r}_i}^2 + V_{ext}(\mathbf{r}_i) + \frac{e^2}{2} \sum_{i \neq j} \frac{1}{|\mathbf{r}_i - \mathbf{r}_j|} = T + V_{ext} + V_{e-e}. \quad (1)$$

The 3 terms in Eq. (1) represent respectively the electron kinetic energy, the ion–electron interaction, and the electron–electron interaction. A direct diagonalization of this Hamiltonian is impossible even for modern computers for most of condensed matter systems. A different approach is therefore necessary. A successful method for the calculation of ground-state properties, such as for example the geometry of the material, or its total energy, makes use of Density Functional Theory (DFT). DFT is based on the Hohenberg and Kohn theorem [1], that states that the ground-state energy of an interacting-electron system is a unique functional of the electronic ground state density $n(\mathbf{r})$. As a consequence, DFT enables to focus the attention on the electronic density $n(\mathbf{r})$ rather than on the more complex many body wavefunction $\Psi(\mathbf{r}_1, \dots, \mathbf{r}_N)$. The Hohenberg and Kohn theorem is valid also for non-interacting electron systems. Kohn and Sham used this fact to demonstrate that the interacting-electron problem can in principle be solved by finding the solutions of a single-particle Schroedinger-like equation [4]

$$\left[-\frac{\nabla_{\mathbf{r}}^2}{2} + V_{ext}(\mathbf{r}) + V_{Hartree}(\mathbf{r}) + V_{xc}(\mathbf{r}) \right] \phi_j(\mathbf{r}) = \varepsilon_j \phi_j(\mathbf{r}). \quad (2)$$

This is the so-called Kohn–Sham (KS) equation. The exchange–correlation potential $V_{xc}(\mathbf{r})$ is a functional of the density, but its analytical expression is unknown. Many approximations (LDA, GGA, ...) [4–6] have been developed for V_{xc} . The Kohn–Sham (KS) equation allows to calculate the charge density n ,

$$n(\mathbf{r}) = \sum_j f_j |\phi_j(\mathbf{r})|^2, \quad (3)$$

where f_j are the occupation numbers, and ϕ_j are the solutions of the KS equation, and derive from it all the other ground-state quantities.

2.1. Dynamics

Dynamical processes of insulators and molecules at room temperature, can be considered with good approximation as occurring by maintaining the electrons in the ground state in all the geometrical configurations visited, since the electronic transition to excited states requires an energy of the order of some eV, that is much larger than $k_B T$, where k_B is the Boltzmann constant. Since DFT is conceived to calculate ground-state properties, it is particularly suited to simulate the dynamics of a condensed matter system.

In the Born–Oppenheimer (BO) molecular dynamics, the ionic degrees of freedom are propagated by Newtonian laws in which forces acting on the atoms are calculated at each iteration as the derivative of the total energy with respect to the ionic coordinates.

This implies that the DFT electronic problem must be solved with conventional matrix diagonalization methods for each step of the dynamics. In contrast, in the most used Car–Parrinello method [7] the electronic degrees of freedom are explicitly introduced as (fictitious) dynamical variables. This is done by writing an extended Lagrangian for the system which leads to coupled equations of motion for both ions and electrons. In this way an explicit electronic minimization at each iteration is not needed: after an initial standard electronic minimization, the fictitious dynamics of the electrons is conceived to keep them near the BO surface for each new ionic configuration visited along the dynamics.

2.2. Excited-state properties

In order to calculate excited state properties, we used two different approaches. The first one is based on Time-Dependent Density Functional Theory (TDDFT) [8,9] that is an extension of DFT to time-dependent domain, and is conceived for example to study optical properties. TDDFT is based on the Runge and Gross theorem [8] that is the analogous of the Hohenberg and Kohn theorem of DFT. The excited states energies can be computed, in linear response regime, as the poles of the response function of the interacting-electron system (the functional derivative of the density charge with respect to the external potential) that can be calculated by a Dyson-like equation:

$$\chi = \chi_{KS} + \chi_{KS}(\nu + f_{xc})\chi, \quad (4)$$

where χ_{KS} is the independent particle response function calculated using KS-equation solutions, ν is the Coulomb potential, and f_{xc} is the exchange and correlation kernel, that is the functional derivative of the exchange–correlation potential with respect to the density. The microscopic dielectric matrix can be easily calculated from the response function. The macroscopic dielectric function is then obtained from the microscopic one [10–13].

TDDFT is formally an exact theory, but, since the analytical form of the exchange–correlation kernel, as well as the exchange–correlation potential, is unknown, some approximations are required. Most of these approximations are local and do not describe the long range part of the exchange–correlation interaction. Therefore TDDFT usually works well for isolated systems (such as molecules, see for example [14]), and special care has to be used in its applications to infinite systems [15], where the electron–electron and electron–hole long range interaction are important. Nevertheless, with appropriate kernels, also surfaces [16] and bulk [17,18] have been recently studied.

The second approach is a combination of two quantum Many-Body Perturbation Theory (MBPT) techniques based on Green's Function Theory: the GW method [10–13], and the Bethe–Salpeter equation (BSE) [19]. The GW method enables to calculate the quasi-particle energies, that are related to the electronic band structure. The GW approximation is derived by setting the vertex in the Hedin equations [20,11] equal to a delta function. Under this condition, the time-Fourier transform of the self energy $\Sigma(\mathbf{r}, \mathbf{r}', \omega)$, becomes a convolution of the Green's function $G(\mathbf{r}, \mathbf{r}', \omega)$ with the screened Coulomb potential $W(\mathbf{r}, \mathbf{r}', \omega)$. The electronic bands can be obtained by solving the following eigenproblem:

$$\left[-\frac{\hbar^2 \nabla_{\mathbf{r}}^2}{2m} + V_{ext}(\mathbf{r}) + V_{Hartree}(\mathbf{r}) \right] \phi_j(\mathbf{r}) + \int d^3 r' \Sigma(\mathbf{r}, \mathbf{r}', \varepsilon_j^{QP}) \phi_j(\mathbf{r}') = \varepsilon_j^{QP} \phi_j(\mathbf{r}), \quad (5)$$

where ε_j^{QP} are the quasi-particle energies (the electronic energy levels) and, as a first approximation for ϕ_j , the Kohn–Sham eigenfunctions can be usually used [21]. The GW method provides a way

to calculate the energy levels but, in order to calculate the optical absorption spectrum, it is necessary to include excitonic effects by solving the BSE [19]. The main ingredients of this equation are the screened Coulomb interaction, W , present in the definition of the BSE kernel \mathcal{E} , and the four-point independent particle polarizability that in transition space takes the form:

$$P_{(n1,n2)(n3,n4)}^0(\omega) = \frac{f_{n2} - f_{n1}}{\varepsilon_{n2}^{QP} - \varepsilon_{n1}^{QP} - \omega} \delta_{n1,n3} \delta_{n2,n4}, \quad (6)$$

where f are the occupation numbers. The polarizability P of the interacting system can be calculated by solving the BSE that can be expressed in the simplified form:

$$P = P^0 + P^0 \mathcal{E} P \quad (7)$$

where \mathcal{E} is the MB kernel. P , the generalized four-point polarizability, is related to the dielectric function from which it is possible to obtain the optical absorption spectrum.

MBPT methods are very accurate also for the prediction of excited-state properties of solids, since the exchange-correlation interactions are non local. Furthermore the presence of two different methods to calculate electron (by GW) and optical properties (by BSE) enables a deeper analysis of the role of the excitonic effect. The drawback with respect to TDDFT methods is the higher computational cost of the GW + BSE approach.

2.3. Large systems (QM/MM approach)

The above methods are all based on quantum mechanics, whose complexity prevents modern computers to treat systems with more than few hundreds atoms (see for example Ref. [22]). Unfortunately, systems of interest can be much larger, especially in biophysics. Nevertheless, most of the times, only a small part of the system needs to be treated at an accurate quantistic level, while the rest can be treated with a more approximated approach, by a classical model. This is the basic idea of Quantum Mechanics/Molecular Mechanics (QM/MM) techniques [23].

In other words, QM/MM enables to separate a condensed matter system in two subsystems. In one of them, the electronic properties are important and have great influence on the dynamics, chemical reactions and the optical properties; therefore this subsystem must be treated quantum mechanically. The second subsystem can instead be described by a classical model where the atoms are replaced by point-charges and the inter-atomic interactions are modeled by harmonic forces. The interface between the two subsystems is more or less complicated depending on the nature of the bonding between QM and MM atoms. In a QM/MM scheme the KS equation takes the following form:

$$\left[-\frac{\hbar^2 \nabla^2}{2m} + V_{ext}^{QM}(\mathbf{r}) + V_{ext}^{QM/MM}(\mathbf{r}) + V_{Hartree}(\mathbf{r}) + V_{xc}(\mathbf{r}) \right] \phi_j(\mathbf{r}) = \varepsilon_j \phi_j(\mathbf{r}) \quad (8)$$

$V_{ext}^{QM}(\mathbf{r})$ is the external potential induced by the ions of the QM atoms, while $V_{ext}^{QM/MM}(\mathbf{r})$ is the external potential induced by the point charges representing the MM atoms. QM/MM allows to treat systems containing thousands of atoms and is mainly used to study the dynamics of chemical reactions, bio-chemical solutions, or molecular dynamics at room temperature.

This technique was also combined with TDDFT in order to calculate excited-state properties [24] of large systems with a small optically active subsystem. In the next section we show an application where the quantum part of a QM/MM calculation has been treated by GW and BSE introducing a QM/MM potential in Eq. (5), following the scheme of Eq. (8). More details on the method are reported in Refs. [25,26].

3. Indole

Amino acids are biologically important organic compounds made from amine ($-\text{NH}_2$) and carboxylic acid ($-\text{COOH}$) functional groups, along with a side-chain specific to each amino acid. The role of the amine and of carboxylic acid is to bind amino acid to each other forming peptidic chains that are the primary structure of proteins. The side chain gives to each amino acid distinctive chemical and physical properties. For most of them, the side chain does not present peaks of optical absorbance in the visible and UV range. This is why proteins are transparent. There are, however, some exceptions represented by amino acids whose side chains has harmonic carbon rings that absorb in this range of frequencies. One of these amino acids is the Tryptophan (Trp). Its side chain is indole, reported in Fig. 1. Indole has been exploited as a spectroscopic tool to monitor changes in proteins and to yield information about their local structure and dynamics. In fact, its spectral signatures allow it to be used as a structural probe in proteins [27].

Here we study the modifications of the indole absorption spectrum induced by the solvent, when indole is in water solution. We perform Car–Parrinello simulations of indole in water. The biomolecule is treated, at a first step, at the DFT level. The solvent is treated by a classical model (MM) as explained in Section 2, and is considered within the Assisted Model Building with Energy Refinement (AMBER) force field. Finally, we calculate the indole absorption spectrum both by TDDFT and by GW and BSE, in water solution and in the gas phase. 20 ps hybrid QM/MM Car–Parrinello simulations [7,23] as implemented in the Car–Parrinello code CPMD3.11.1 [28] are used for indole in water. We consider one indole molecule (QM-part) surrounded by 1376 classical water molecules (MM-part). The forces acting on classical atoms are calculated according to the Parm99 version of AMBER force field [29] that is parametrized according to the three-site transferrable intermolecular potential (TIP3P) [30] for water molecules. The time step chosen for the simulations is of about 0.1 fs. The electrostatic interactions between periodic images of the QM-part is decoupled by the scheme of Martyna–Tuckerman [31]. Such a large number of molecules are required to reproduce correctly the physical properties of a disordered system such as liquid water at room temperature and pressure [32].

For ten snapshot of the QM/MM dynamics (one every two ps) we compute the optical spectra at the independent particle level (IP-RPA), by TDDFT within the Tamm–Dancoff approximation [33] as implemented in the CPMD3.11.1 [28], and by GW and BSE. In particular, for TDDFT we use PBE [5] exchange–correlation functional, since BLYP is known to be not very accurate for linear response calculations especially in a plane wave basis set scheme (also for PBE,

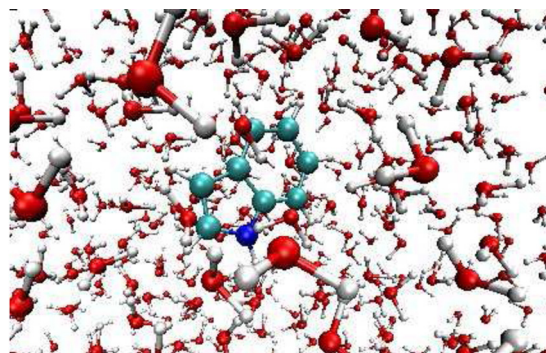


Fig. 1. Indole. Colors corresponds to the following atomic species: BLUE=N, CYAN=C, WHITE=H, and RED=O. (For interpretation of the references to color in this figure legend, the reader is referred to the web version of the article.)

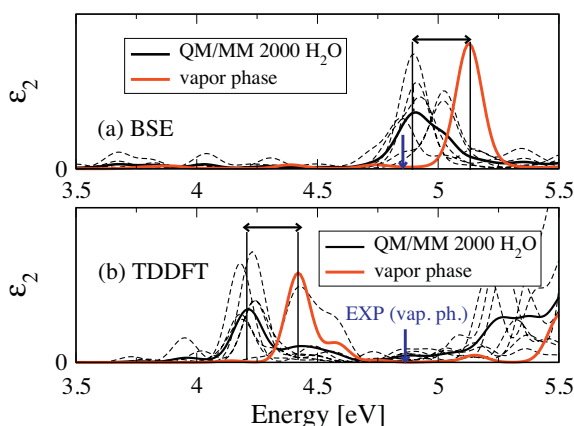


Fig. 2. TDDFT and MBPT (GW + BSE) spectra: the tiny black dashed lines are for the spectrum of each snapshot. The black continuous line is obtained by an average over these spectra. The red dashed line is for indole in vapor phase. (For interpretation of the references to color in this figure legend, the reader is referred to the web version of the article.)

the Trouiller–Martins pseudopotentials are corrected for a better description of Van der Waals interactions [34]). GW calculations have been done by using 12,077 plane-waves and 500 electronic bands. We used periodic boundary conditions and a cutoff in real space for the Coulomb potential to prevent periodic images to interact with each other. The screening function is calculated within a plasmon pole approximation. For BSE calculations we used codes developed within the ETSF European Infrastructure [82]. The BSE was solved by diagonalizing the excitonic Hamiltonian with the inclusion of the coupling part [25]. We used 12,077 plane waves for the wavefunctions, 257 for the local fields and 5100 quasi-particle transitions. We use periodic boundary conditions with a cutoff in real space for the Coulomb potential.

The final spectrum is obtained by an average over the snapshots. The convergence of the spectrum is reached already after 6 snapshots. We observe an average HOMO–LUMO DFT band gap of 3.5 eV.

The optical gap of indole is about 3 eV smaller than water one (7 eV [35–37]), and therefore the spectra of these two systems do not overlap at low frequencies. This could explain why the spectrum of indole in water can be calculated by considering water molecules by a classical model (MM), as has been proved by some tests we did with water molecules treated by QM and giving the same spectrum at low energies.

In Fig. 2 we report the spectra of indole in water and in vapor phase calculated by TDDFT and MBPT. From experimental observations we know that the most intense peak of the lower part of the optical spectrum is at 4.77 eV (1L_a) [35,36]. This peak is visible at 4.4 eV in the TDDFT spectrum and 4.9 eV in the MBPT spectrum.

We find, in agreement with experiments [38–40], a red shift of the optical spectrum when going from vapor phase to solution. The value of the theoretical solvent shift obtained by both TDDFT/MM and MBPT/MM is 0.2 eV. The experimental value for 1L_a state is 0.18 eV [38]. In previous theoretical calculations [39] based on (CAS)SCF method and CASPT2, the solvent is simulated by a continuum model with a cavity containing the indole molecule and a shift of 0.06 eV is obtained. We believe that this underestimation depends on the fact that the geometrical distortion of indole molecule is not considered in these works since the calculations are performed with relaxed coordinates, but without performing a dynamical simulation in water.

In order to better understand the importance of the geometry distortion we perform calculations of indole switching on and off the water field, to be able to separate the geometry effect from the

electrostatic one. We calculate the spectrum of indole at the IP-RPA level for 8 snapshots without water field. The average spectrum is red-shifted of about 0.1 eV compared to the spectrum of indole in vapor phase. This indicates that the geometrical distortion induces a red shift in the lower part of the spectrum that is further increased by the water field effect.

This shift is a consequence of the combination of both the effects: the geometrical distortion of indole molecule in the solvent and the electrostatic interaction with the water molecules electric dipoles. TDDFT/MM is a well established method and works quite well for most of the molecules. MBPT/MM has been applied for the first time in this work. TDDFT gives in this case a small underestimation of the optical gap by 0.4 eV with respect to the experiment while MBPT overestimate it by 0.3 eV, but both methods give the same value of the solvatochromic shift that is in very good agreement with the experiment.

4. Protonated Schiff Base Minimal Model

tZt-penta-3,5-dieniminium cation ($C_5H_6NH_2^+$) is the smallest model molecule for the 11-CIS retinal of the rhodopsin that is the chromophore acting as a receptor of light signals in animals eyes. This is the reason why it is also called Protonated Schiff Base Minimal Model (PSBMM). It is a photo-active molecule, since the absorption of a photon induces its isomerization. This photoisomerization is the first step sight mechanism. As for the retinal, the photoisomerization of the PSBMM can be qualitatively described by a two-state model [41] (see Fig. 3). According to this model (lower panel, Fig. 3), the ground state of the Schiff Base has two minima corresponding to CIS and TRANS conformations. A rotation of the molecule around the axis connecting the two internal carbon atoms breaks the double bond between them, and induces an increase of the total energy that reaches its maximum after a rotation of about 90°. CIS and TRANS ground state energies are therefore separated by a barrier of about 2 eV. On the contrary, the first excited singlet state S_1 has an energy of about 4 eV [42] above the ground state in CIS and TRANS configurations, and decreases in rotated geometrical conformations. The minimal energy corresponds to a rotation of about 90° at which a conical intersection (CI) between the S_0 and S_1 surfaces occurs. The minimal energy path of the isomerization does not correspond to a rigid rotation of the dihedral angle reported in Fig. 3, but undergoes first an elongation of the C_2 – C_3 bond whose maximal velocity is reached in correspondence of the hypersphere energy minimum HM

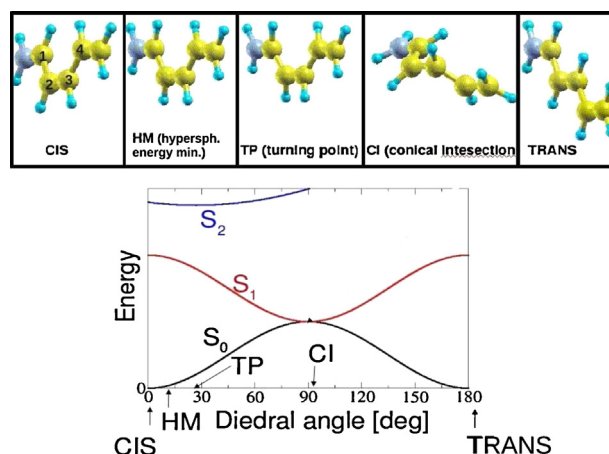


Fig. 3. Upper panel: main geometry configurations of the Protonated Schiff Base Minimal Model during its isomerization. Lower panel: qualitative description of the two-state model. The dihedral angle is the one formed by the atoms labeled 1, 2, 3 and 4 in the upper panel.

configuration, and stops in correspondence of the TP configuration after which the isomerization becomes almost a pure rotation.

A second more complicated model is also possible involving the S_2 state, that could form a second conical intersection with the S_1 state inducing a small energy barrier in the S_1 state along the path connecting the CIS conformation to the S_0 – S_1 conical intersection. This barrier could modify the velocity of the isomerization, but does not change the nature of the process.

Despite the small size of the PSBMM, the qualitative description of its photoisomerization is not easy to simulate. Some efforts to predict the photoisomerization trajectory using TDDFT failed because of the inability of most of the approximations for the exchange–correlation kernel to correctly compute the excited-state forces of Schiff Bases [43]. A common strategy to calculate the excitation energies of the PSBMM is to use CASSCF derived geometries [42,44].

After the determination of the trajectory, the second problem to cope with is the calculation of the excited state energies, and, once again, different methods give different results, even when the same coordinates are used [44]. This is evident by comparing post-Hartree Fock based CASPT2 [42,44], Diffusion Monte Carlo (DMC) [45], and TDDFT excited state energies [43].

In Ref. [44], CASPT2 calculations performed on a CASSCF-trajectory find a very small barrier (<0.1 eV) along the isomerization pathway. Apparently, no energy barrier is found within Diffusion Monte Carlo calculations performed on ROKS minimal energy path (MEP) [45] although this observation should be verified by a calculation of the S_1 energies on a more dense sampling. A higher barrier was found by using TDDFT both on CASSCF [44] and on ROKS [45] coordinates. The difference with CASPT2 outcomes is that the S_1 energy of the geometrical configuration corresponding to the top of the energy barrier has an higher energy than S_1 CIS energy. This could strongly affect an excited state dynamics of the system. Given the importance of the geometry on the optical properties of the PSBMM, the different choice of coordinates introduces a further complication for the task of comparing the results between various methods and interpret their dissimilarities. The few available experimental data cannot provide any help [46–48]: at best of our knowledge, experimental optical spectra are at present available only for molecules with a similar structure (but not exactly the same) and not for molecules in gas phase, but only in solution or in solid-state phase. Moreover, no experimental information is available on the intermediate configurations, but only on the CIS one.

The discrepancies between TDDFT calculations and CASPT2 are generally attributed to the inability of most of the approximations used in TDDFT to correctly describe the electron–hole interaction in charge-transfer materials. This interaction is better treated by quantum Many-Body techniques such as the GW method [10] combined with the Bethe–Salpeter equation (BSE) [19,49].

In Fig. 4 we show the results of Ref. [50] of calculations of the optical absorption spectra and ground and excited-state energies of the Minimal Model by GW and BSE on representative geometrical configurations along the photoisomerization pathway. The atomic coordinates were taken from Ref. [42] and are calculated by CASSCF. For both MBPT and TDDFT we used the same coordinates. Our results are in qualitative agreement with CASPT2 and quantum Monte Carlo observations: no energies higher than CIS configuration are found along the S_1 minimal energy path going from CIS to CI.

We observe a decrease of the intensity of the first two peaks of the optical absorption spectrum (see Fig. 4) induced by the distortion of the planar geometry of the PSBMM along the isomerization path. This trend is inverted in proximity of the conical intersection where the first peak intensity increases enormously due to the S_0 – S_1 states degeneracy. But in the first stages of the

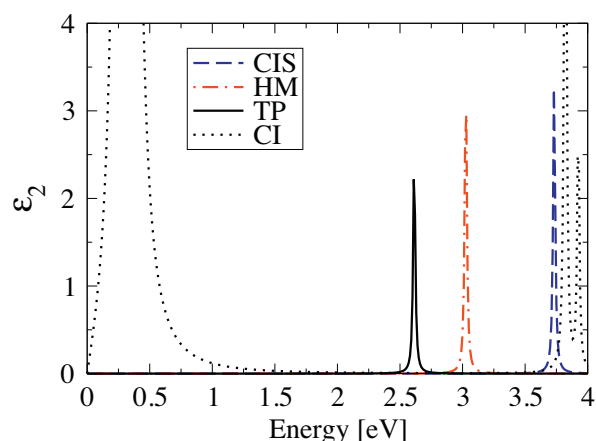


Fig. 4. Optical absorption spectrum of the PSBMM calculated by GW and BSE, in four different geometrical configurations along the minimal energy path: CIS, HM, TP, and CI displayed in Fig. 3.

isomerization, this tendency is quite evident. This point could be interesting from an engineering point of view. It is well known actually that similar photo active molecules, as for example the retinal of rhodopsin, located in our eyes, absorb light optical signals and transform photons in electrical signals to be sent to the brain throughout the optical nerve where images are elaborated. It would be worth to try to use this same process to build cells based on photo active molecules to convert solar energy into electricity. One of the problems of solar cells is that the process of conversion must be faster than the hole–electron recombination. The best devices are therefore those where the spontaneous emission is reduced to the minimum. The information that we give in this work is that a geometrical distortion of the PSBMM induces a decreasing of the absorption peaks, and therefore reduces also the probability of a spontaneous emission event. Of course this also reduces the quantum efficiency of the device, that can anyway be compensated by increasing the number of photo active molecules in the device.

The construction and engineering of a solar cell is very complex and the absorption of the photons is just a small aspect of all the operating mechanism. Anyway, if our results about the strong dependence of the intensity of the absorption optical spectrum will be validated also by other methods, this information could be of some help for the construction of organic solar cells of the next generation.

5. Si(1 1 1)2 × 1

The Si(1 1 1)2 × 1 is one of the most investigated surfaces ever but some issues are still not completely understood. The 2 × 1 reconstruction is observed when Si samples are cleaved along a (1 1 1) surface in Ultra High Vacuum. An appropriate model for the atomic structure of this reconstructed surface is the Pandey model [51] with a little buckling of the topmost atoms. According to the Pandey model, rows of π -bonded atoms (Pandey chains) are present in the first atomic layer. Two different geometric configurations (called isomers) can be distinguished in relation to the (conventional) sign of the buckling: the positive buckling and the negative buckling (see Fig. 5). It is currently believed that Si(1 1 1)2 × 1 buckles in a positive sense at room temperature [52] but recently it has been demonstrated, by a comparison between experimental and theoretical Scanning Tunneling Spectroscopy (STS), that both the isomers occur on the surface for highly n-doped samples at low temperature [53] and even at room temperature [54]. A deeper study of the geometric, electronic and optical

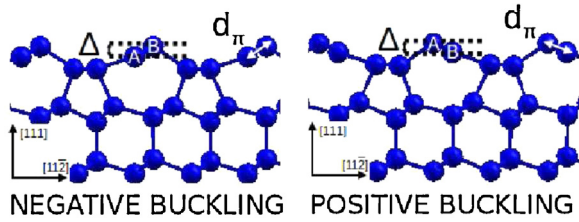


Fig. 5. Side view of both the isomers of Si(1 1 1)2 \times 1. The distance d_π between atom A and atom B is the bond length along the Pandey chain; the difference in height between atom A and atom B, Δ , is the buckling amplitude.

properties of positive and negative buckling is hence needed to further investigate and finally confirm the coexistence of the isomers.

To model the isomers we apply the supercell method using slabs of 24 atoms (12 atomic layers) separated by 7.42 Å of vacuum for structural and energetic properties and by 17.12 Å of vacuum for electronic and optical properties.

Within DFT–LDA, using 30 Ry of cutoff energy and 100 k -points in the Irreducible Brillouin Zone (IBZ), we obtain the ground state geometries of both the isomers. We find a buckling amplitude Δ of +0.53 Å for the positive buckling and of –0.59 Å for the negative buckling (see Fig. 5). These values are in good agreement with the most recent theoretical results [53,55]. Concerning the bond length along the Pandey chains, we obtain $d_\pi = 2.27$ Å for both the isomers (see Fig. 5).

We find that the two isomers are both local energetic minima and they are separated by an energetic barrier of nearly 0.06 eV/(2 \times 1) (upper limit value). In our calculations the total energy of two isomers differ of only about 5.4 meV/(2 \times 1), hence the two isomers can be considered degenerate within the DFT–LDA accuracy, as reported in previous works [53,56,57].

Concerning the electronic properties, we have made calculations within DFT–LDA, using 20 Ry of cutoff energy and 231 k -points in IBZ, and within Many Body Perturbation Theory in the GW approximation, using 231 q -points in IBZ, 1977 plane waves and 452 empty bands for the screening, 4979 plane waves for Σ_c , 1977 plane waves and 452 empty bands for Σ_v . In Fig. 6 we show the electronic band structure for both the isomers of the Si(1 1 1)2 \times 1 along the $\bar{J}\bar{K}$ direction (that is, around the fundamental gap).

GW minimum gaps are reported in Table 1; these values are in very good agreement with the most recent STS experimental data [53] (0.83 eV for the positive buckling and 0.47 eV for the negative buckling).

Concerning the optical properties, we have focused on RAS (Reflectance Anisotropy Spectroscopy) spectra. RAS [58,59] is a powerful experimental technique widely used to study and

Table 1

Theoretical electronic (GW) and optical properties (within the BSE) of the Si(1 1 1)2 \times 1 negative buckling (NB) and positive buckling (PB).

	Electronic gap [eV]	Optical gap [eV]	Excitonic binding energy [eV]	Excitonic radius [Å]
NB	0.44	0.31	0.13	>80
PB	0.77	0.45	0.32	~80

characterize surfaces (see for example [60]). The RAS signal measures the difference of reflectivity for light polarized along two perpendicular directions (x and y) on the surface:

$$\frac{\Delta R}{R} = \frac{R_y - R_x}{R}$$

and it corresponds to the difference of the reflectivity corrections to the Fresnel case for the two different light polarizations. For cubic crystals, the RAS signal comes from the surface anisotropy, since the bulk is optically isotropic. If the surfaces are modeled by the supercell method, there is a simple theoretical expression for the RAS spectrum, involving the half-slab polarizability α_{ii}^{hs} and the bulk dielectric function ϵ_b :

$$\frac{\Delta R}{R} = \frac{4\omega d}{c} \text{Im} \frac{4\pi\alpha_{ii}^{hs}}{\epsilon_b - 1}$$

where d is the half-slab thickness, and i is the direction of light polarization.

Half-slab polarizability α_{ii}^{hs} and bulk dielectric function ϵ_b have been calculated in the Random Phase Approximation using DFT–LDA. In the present work, y (x) is the direction parallel (perpendicular) to the Pandey chains. Details of the calculations are reported in Ref. [61].

In Fig. 7 we show the RAS spectra of positive and negative buckling isomers, within DFT–LDA, up to 6 eV: there are differences concerning the shape, the intensity and the position of the peak. The Si(1 1 1)2 \times 1 negative buckling presents a RAS peak (0.23 eV) at lower energies with respect to the positive buckling (0.48 eV) and this is related to the differences in the DFT gap values (see Fig. 6). Moreover the peak is more intense for the negative buckling isomer: this is related to the different gaps and to the fact that the empty and occupied surface bands are parallel in a wider region along the $\bar{J}\bar{K}$ line for the negative buckling with respect to the positive buckling.

The results obtained for the Si(1 1 1)2 \times 1 positive buckling are in agreement with previous DFT–LDA RAS spectra [16]; the red shift of the negative buckling RAS peak with respect to the positive buckling was already predicted in [55].

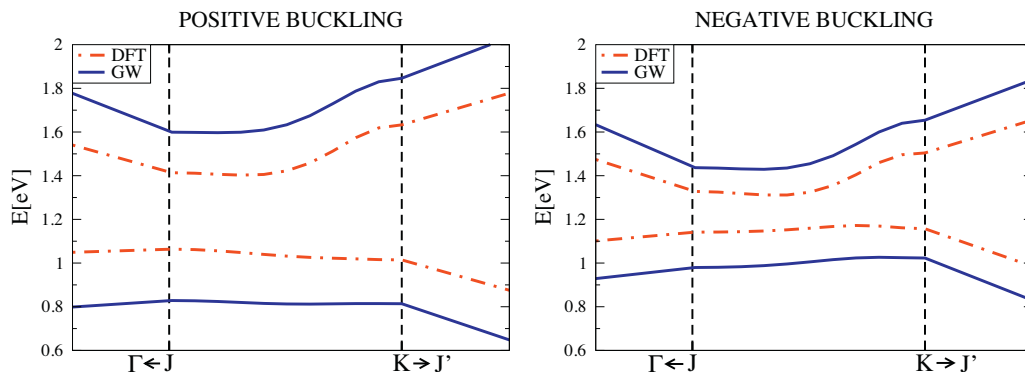


Fig. 6. Electronic band structure around the fundamental gap of both the isomers of Si(1 1 1)2 \times 1 obtained within DFT–LDA (red dashed lines) and within GW (blue solid lines). (For interpretation of the references to color in this figure legend, the reader is referred to the web version of the article.)

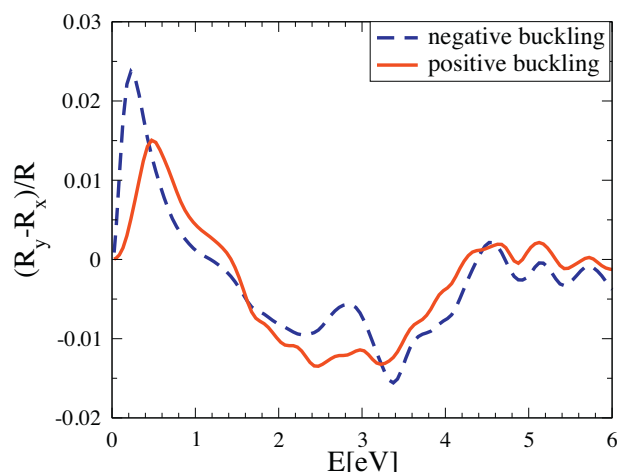


Fig. 7. RAS spectra of Si(1 1 1)2 × 1 positive buckling (red solid line) and negative buckling (blue dashed line) calculated within DFT–LDA. y is the direction parallel to the Pandey chains and x is the direction perpendicular to the chains. (For interpretation of the references to color in this figure legend, the reader is referred to the web version of the article.)

We can observe that the optical response of the two configurations is deeply different: this can be exploited to distinguish the two isomers in RAS experiments. For a quantitative and qualitative comparison with the experimental data, the introduction of the excitonic effect is necessary; this can be done by solving the BSE [62,16] and within TDDFT [16] calculations only for the positive buckling; for this isomer many experiments concerning RAS spectra are present in literature [63,64]. A calculation of the RAS spectrum of the negative buckling with the inclusion of the effects correlated to the electron–hole interaction is still missing. As far as we know, in literature there is only a hybrid DFT calculation [55] concerning the negative buckling and there are no experiments.

We have performed optical calculations for both the isomers with the inclusion of the excitonic effects: the optical gaps are reported in Table 1. The value of the optical gap for the positive buckling is in excellent agreement with the experiments [63,64] and so we can assume the reliability of the optical gap of the negative buckling. The optical gaps are different, so experiments could actually distinguish the two isomers. We can also remark the differences concerning the properties of the lowest energy surface exciton (the one that dominates the optical spectrum) between the two configurations (see Table 1): the negative buckling is more delocalized along the Pandey chains because of its lower binding energy with respect to the positive buckling isomer, for which we have estimated an excitonic radius of nearly 80 Å.

The importance of the differences between the optical gaps and the surface excitons of the two isomers, highlighted previously, are connected to the possibility to exploit them to further investigate the coexistence of the two configurations at different temperatures and levels of doping, comparing experimental RAS spectra of Si(1 1 1)2 × 1 to the theoretical results.

6. Paper

Paper is a complex multi-component material consisting mainly in a network of cellulose fibers derived from plants in ancient times and from wood pulp today.

Cellulose is the most common organic compound on Earth, representing 40% of the annual production of biomass [65]. It is made of several hundred to over thousands units of

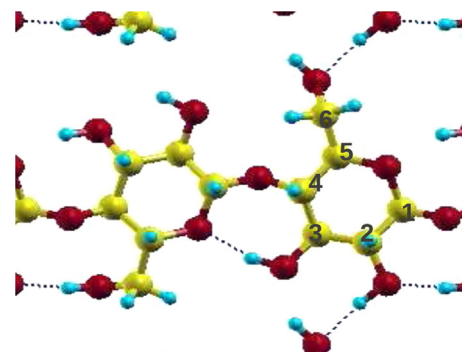


Fig. 8. Structure of cellulose crystal. Yellow, red, and cyan balls correspond respectively to C, O, and H atoms. Blue dashed lines indicate H-bonds. (For interpretation of the references to color in this figure legend, the reader is referred to the web version of the article.)

β -(1,4)-D-glucopyranose (Fig. 8) arranged by hydrogen bond in crystalline domains and amorphous regions [66–68].

Paper degradation on aging occurs by the weakening of mechanical properties of the sheets and by yellowing. These phenomena are caused by a combination of two interdependent degradation routes: (a) acid hydrolysis of the cellulose polymeric chains, which weaken the mechanical properties of the sheets [65,69] and (b) oxidation of materials with subsequent development of chromophores and other byproducts, and discoloration of the remaining substratum [69–71]. Cellulose oxidation running through the radical mechanism initiated by active oxygen species is a complex process giving final products still to be clarified [69,72–75].

From an optical point of view the moderate oxidation of cellulose causes the formation of a broad absorption band peaked around 4.8 eV (260 nm), and a long absorption tail extending up to the visible region. The absorption peak at 4.8 eV has been attributed to the development of carbonyl groups through the comparison of the spectra of similar compounds [76,72–74]. However, because of the important role of the local chemical environment in the cellulose molecular crystal, this procedure does not allow to distinguish, for example, between ketones and other enolic groups in the oxidized cellulose.

A detailed knowledge of the oxidation products of cellulose in aging could shed light to the mechanisms in play during paper degradation, useful for the improvement of conservation and restoration practises of ancient piece of art on paper.

In this section, we present recent results and progresses obtained in the comprehension of the role of cellulose oxidation in the yellowing of ancient paper with the aid of Time-Dependent Density Functional Theory (TDDFT) calculations [8,77].

In this research work we concentrate on paper produced in the Middle Ages, in particular during the 14th and 15th centuries in the Mediterranean area, as reported in Table 2.

The absorbance (A_{KM}) of ancient paper samples was obtained by applying the Kubelka–Munk (KM) model to diffuse reflectance measurements [78,79]. Ultraviolet–visible–near infrared (UV–vis–NIR) diffuse reflectance spectra were measured at room temperature and at 50% of relative humidity (RH) conditions by using a Jasco V-570 spectrophotometer

Table 2

List of all the Middle Ages samples measured in the experiments.

Sample label	Provenance	Production date
A1	Perpignan (France)	1413
A2	Milan (Italy)	1430
A3	Milan (Italy)	1430
529	Damascus (Syria)	1300–1350
17	Damascus (Syria)	1300–1350

Table 3

List of the simulated cellulose's oxidized forms.

Oxidized group	Description
CCO	Complete oxidation of C(6) with carboxylic group and a double bond C(5)=C(6)
CHO	Oxidation of C(6) with the formation of an aldehydic group
M2H	Oxidation to a single ketone on C(2)
M4H	Conjugated diketones on C(2) and C(3)
CC	Formation of a double bond C(5)=C(6)

equipped with an integrating sphere and a PbS detector or by using an Avantes set-up formed by an AvaLight-DH-S-BAL light source, an AvaSphere-30-REFL integrating sphere and an AvaSpec-2048x14-USB2 spectrometer. All measured spectra were normalized to a Spectralon diffuse reflectance reference standard (factory calibrated). The spectra resolution was set to 2 nm in both the experimental set-up. Paper samples were measured over two backgrounds, one with reflectance close to 1 (white), and another with reflectance close to 0 (black), while the backgrounds reflectance were measured separately. The KM model allows to convert the reflectance of a sample over the two backgrounds into the reflectance R_{inf} that would have an infinite layer of the same sample. Once calculated R_{inf} , it is possible to recover the KM absorbance A_{KM} as

$$A_{\text{KM}} = \frac{(1 - R_{\text{inf}})^2}{2R_{\text{inf}}} \quad (9)$$

for comparison with TDDFT simulations [79].

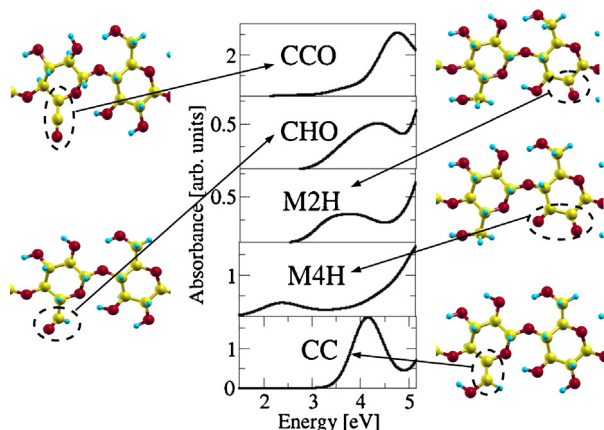
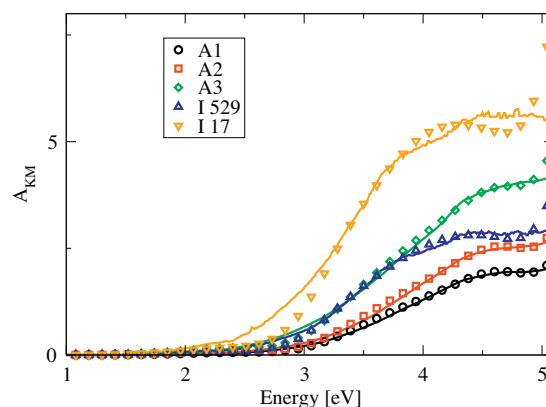
We have calculated the macroscopic dielectric function of cellulose by using the Casida algorithm [80] within a TDDFT framework with a gradient-corrected local approximation (BLYP) [6] for the exchange-correlation potential. The theoretical absorbance has then been obtained by the expression:

$$\alpha = 2\omega \sqrt{\frac{\sqrt{\varepsilon_1^2 + \varepsilon_2^2} - \varepsilon_1}{2}}, \quad (10)$$

where ε_1 and ε_2 are respectively the real and the imaginary part of the dielectric constant, and then compared to the experimental value A_{KM} .

We have considered several possible oxidized forms of cellulose which have been supposed to give absorption effects in the visible range [72–74]. These are shown in Fig. 9 and are named as reported in Table 3.

As a structural model for the simulation of optical properties we have chosen an infinite crystal of cellulose as an approximation of cellulose crystalline domains. Cell parameters of the cellulose

**Fig. 9.** Theoretical absorbance spectra of oxidized groups.**Fig. 10.** Experimental absorbance A_{KM} (solid line) and corresponding theoretical absorption spectra (symbols) of the Middle Ages' paper samples.

crystal were taken from X-ray diffraction data [65] and refer to the monoclinic crystallographic phase called cellulose- I_β [65,66]. The atomic coordinates inside the cell, containing 42 atoms, were theoretically calculated by the QUANTUM ESPRESSO plane-wave DFT code.

Further theoretical details on the method used are reported in Ref. [77]. In Fig. 10 we report A_{KM} for all ancient samples. The absorbance has a maximum value at the high energy side of the measured spectra around 4.8 eV (260 nm), indicating development of carbonyl groups in glucopyranose units [76]. At lower energies it smoothly decreases with a tail extending up to the beginning of the visible energy region between 2 and 3 eV.

The wide energy range of the spectral region of absorbance suggests the presence of several chromophores of different nature.

The calculated optical absorption spectra do not present absorption below 5.1 eV for pure cellulose, in agreement with the experiments. The oxidized groups, instead, are characterized by the appearance of maxima between 2 and 5 eV as shown in Fig. 9. The hole–electron charge distribution related to these peaks is mainly localized on the double bonds induced by the oxidation. Because of this strong localization the optical absorption spectrum below 5 eV of every oxidized group can be considered as produced by several isolated non-interacting chromophores, which are responsible for the yellowing of paper [73,74,77]. Above 5 eV, instead, bands due to oxidized groups are superimposed with the fundamental absorption of the host material (cellulose) [77].

As a consequence, a minimal square algorithm could be applied to extrapolate the chromophores' relative concentrations by a comparison with the experimental spectra.

In Fig. 10, the symbols represent the linear combination of chromophores' spectra that better reproduce the experimental spectrum obtained by the minimal-square based algorithm carried out in the energy range 1.5–5.1 eV.

A very good agreement between calculated and experimental spectra is found for all samples.

By normalizing the linear combination coefficients of theoretical spectra it is possible to recover the relative concentrations of chromophores (Fig. 11).

Our calculations are able to identify the most significant structures observed in the experimental spectra. M4H was predicted to be the most significant oxidation causing paper yellowing [72–74] and to be the only one active in the UV–vis wavelength range. Instead, we show that other oxidized groups in cellulose are optically active [77].

In ancient samples with moderate degradation, CHO has been found to be the most abundant oxidized group. The increasing intensity of A_{KM} absorbance can be accounted for by the increasing

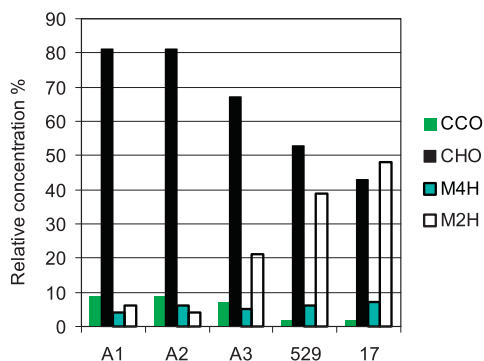


Fig. 11. The relative concentration of the 4 oxidized groups (CC is not reported since it never gives contribution) acting as chromophores as calculated from simulations for Middle Ages's samples.

relative contribution of ketones M2H (see Fig. 11). This increasing is even larger in Damascus samples 529 and 17 (see Table 2), where the relative concentrations of M2H and CHO are comparable. Other studies have shown that this result is typical for samples aged in high humidity environment [77,81]. We also note that CC oxidized group is always absent in all the samples. Therefore, these information on the relative concentrations of chromophores can be used as an indicator of the conservation history and of the state of degradation of ancient paper.

We related optical reflectivity experimental spectra of aged paper to the chemical transformation that caused yellowing by a comparison with theoretical simulations based on TDDFT. We identified the oxidized groups mainly responsible of visual damages in aged paper and observed that the formation of some of these groups is favored by some particular conservation conditions. These results allow to set-up a totally non-invasive and non-destructive diagnostic procedure to get hints on the state of degradation of ancient and unique cultural properties made of, or supported on, paper. This knowledge could be also used for the generation of a new class of bleaching and reducing agents to be employed in paper restoration or in the pulp and paper industry.

7. Conclusions

We reviewed some ab initio techniques for the calculation of electronic and optical spectroscopic properties. We showed that their range of applications goes from isolated molecules, to surfaces, and from bulk periodic systems, to large systems with thousand of atoms whose properties are calculated thanks to hybrid quantum/classical (QM/MM) techniques. We enhanced in some cases their limits and the opportunity to use one method rather than an other in some specific systems. For each example we tried to put the accent on the information that can be extracted from this kind of calculations that is difficult to obtain in other ways.

Acknowledgments

We acknowledge CPU time granted by CINECA, and funding from the EC's FP7 grants no. 211956 (ETSF [82] user projects 211, 71, and 232) and from IC-RCPAL (Italian Minister for Cultural Heritage). We are also grateful to the Library of the Accademia Nazionale dei Lincei and Corsiniana for the measurements on ancient books.

References

[1] P. Hohenberg, W. Kohn, *Phys. Rev.* 136 (1964) B864.
[2] O. Pulci, P. Gori, M. Marsili, V. Garbuio, R.D. Sole, *Eur. Phys. Lett.* 98 (2012) 37004.

[3] See for example O. Pulci, P. Gori, M. Marsili, V. Garbuio, A.P. Seitsonen, F. Bechstedt, A. Cricenti, R.D. Sole, *Phys. Status Solidi A* 207 (2010) 291.
[4] W. Kohn, L.J. Sham, *Phys. Rev.* 140 (1965) A1133.
[5] J.P. Perdew, K. Burke, M. Ernzerhof, *Phys. Rev. Lett.* 77 (1996) 3865.
[6] W.Y.A.D. Becke, C. Lee, R.G. Parr, *Phys. Rev. B* 37 (1988) 785.
[7] R. Car, M. Parrinello, *Phys. Rev. Lett.* 55 (1985) 2471.
[8] E. Runge, E.K.U. Gross, *Phys. Rev. Lett.* 52 (1984) 997.
[9] M.A.L. Marques, E.K.U. Gross, *Time-Dependent Density Functional Theory*, Springer-Verlag, Berlin/Heidelberg, 2003.
[10] A.L. Fetter, J.D. Walecka, *Quantum Theory of Many-Particle Systems*, McGraw-Hill, San Francisco, 1971.
[11] L. Hedin, S. Lundqvist, *Solid State Physics: Advances in Research and Application*, vol. 23, Academic Press, New York, 1969.
[12] G. Onida, L. Reining, A. Rubio, *Rev. Mod. Phys.* 74 (2002) 601–659.
[13] S. Albrecht, L. Reining, R. Del Sole, G. Onida, *Phys. Rev. Lett.* 80 (1998) 4510–4513.
[14] E. Cannuccia, O. Pulci, R.D. Sole, M. Cascella, *Chem. Phys.* 389 (2011) 35–38.
[15] F. Sottile, V. Olevano, L. Reining, *Phys. Rev. Lett.* 91 (2003) 056402.
[16] O. Pulci, A. Marini, M. Palummo, R.D. Sole, *Phys. Rev. B* 82 (2010) 205319.
[17] P. Gori, M. Rakel, C. Cobet, W. Richter, N. Esser, A. Hoffmann, R.D. Sole, A. Cricenti, O. Pulci, *Phys. Rev. B* 81 (2010) 125207.
[18] R.D. Sole, O. Pulci, V. Olevano, A. Marini, *Phys. Status Solidi B* 242 (2005) 2729.
[19] G. Onida, L. Reining, A. Rubio, *Rev. Mod. Phys.* 74 (2002) 601.
[20] L. Hedin, *Phys. Rev.* 139 (1965) A796–A823.
[21] O. Pulci, F. Bechstedt, G. Onida, R.D. Sole, L. Reining, *Phys. Rev. B* 60 (1999) 16758.
[22] L.E. Ramos, E. Degoli, G. Cantele, S. Ossicini, D. Ninno, J. Furthmüller, F. Bechstedt, *J. Phys. Condens. Matter* 19 (2007) 466211.
[23] E. Carter, J. Hynes, *J. Chem. Phys.* 94 (1991) 5961.
[24] M. Sulpizi, P. Carloni, J. Hutter, U. Rothlisberger, *Phys. Chem. Chem. Phys.* 5 (2003) 4798.
[25] A.M. Conte, E. Ippoliti, R.D. Sole, P. Carloni, O. Pulci, *J. Chem. Theory Comput.* 5 (2009) 1822–1828.
[26] A.M. Conte, E. Ippoliti, R.D. Sole, P. Carloni, O. Pulci, *Phys. Status Solidi B* 247 (2010) 1920–1924.
[27] D. Creed, *Photochem. Photobiol.* 39 (1984) 537.
[28] J. Hutter, A. Alavi, T. Deutsch, P. Ballone, M. Bernasconi, P. Focher, S. Goedecker, M. Tuckerman, M. Parrinello, CPMD, Max-Planck-Institute für Festkörperforschung/IBM Research Laboratory, Stuttgart/Zürich, 1993.
[29] D.A. Pearlman, P.A. Case, J.W. Caldwell, W.S. Ross, T.E. Cheatham, S. Debolt, D. Ferguson, G. Seibel, P. Kollman, *Comput. Phys. Commun.* 91 (1995) 1.
[30] W.L. Jorgensen, J. Chandrasekhar, J.D. Madura, R.W. Impey, M.L. Klein, *J. Chem. Phys.* 79 (1983) 926.
[31] G.J. Martyna, M.E. Tuckerman, *J. Chem. Phys.* 110 (1999) 2810.
[32] A.M. Conte, V. Garbuio, M. Marsili, E. Ippoliti, R.D. Sole, *Proceedings CSFI08*, in 'Nuovo Cimento C', vol. 32, 2009, p. 73.
[33] S. Hirata, M. Head-Gordon, *Chem. Phys. Lett.* 314 (1999) 291.
[34] O.A. von Lilienfeld, I. Tavernelli, U. Rothlisberger, D. Sebastiani, *Phys. Rev. Lett.* 93 (2004) 153004.
[35] G.D. Kerr, R.N. Hamm, M.W. Williams, R.D. Birkhoff, R.L. Painter, *Phys. Rev. A* 5 (1972) 2523.
[36] R.L. Painter, R.N. Hamm, E.T. Arakawa, R.D. Birkhoff, *Phys. Rev. Lett.* 21 (1968) 282.
[37] V. Garbuio, M. Cascella, L. Reining, R.D. Sole, O. Pulci, *Phys. Rev. Lett.* 97 (2006) 137402.
[38] H. Lami, *J. Chem. Phys.* 67 (1977) 3274.
[39] L. Serrano-Andres, B.O. Roos, *J. Am. Chem. Soc.* 118 (1996) 185.
[40] D.M. Rogers, J.D. Hirst, *J. Phys. Chem.* 107 (2003) 11191.
[41] T. Kobayashi, T. Saito, H. Ohtani, *Nature* 414 (2001) 531.
[42] M. Garavelli, P. Celani, F. Bernardi, M.A. Robb, M. Olivucci, *J. Am. Chem. Soc.* 119 (1997) 6891.
[43] M. Wanko, M. Gavernelli, F. Bernardi, T.A. Niehaus, T. Frauenheim, M. Elstner, *J. Chem. Phys.* 120 (2004) 1674.
[44] S. Fantacci, A. Migani, M. Olivucci, *J. Phys. Chem. A* 2003 (2004) 1208.
[45] F. Schautz, F. Buda, C. Filippi, *J. Chem. Phys.* 121 (2004) 5836.
[46] M. Arnaboldi, M.G. Motto, K. Tsujimoto, V. Balogh-Nair, K. Nakanishi, *J. Am. Chem. Soc.* 101 (1979) 7082.
[47] V. Balogh-Nair, J.D. Karriker, B. Honig, V.K.M.G. Motto, K. Nakanishi, R. Sen, M. Sheves, M. Arnaboldi, K. Tsujimoto, *Photochem. Photobiol.* 33 (1981) 483.
[48] R.F. Childs, G.S. Shavs, R.E. Wasylshen, *J. Am. Chem. Soc.* 109 (1987) 5362.
[49] L. Reining, V. Olevano, A. Rubio, G. Onida, *Phys. Rev. Lett.* 88 (2002) 066404.
[50] A.M. Conte, L. Guidoni, R.D. Sole, O. Pulci, *Chem. Phys. Lett.* 515 (2011) 290.
[51] K.C. Pandey, *Phys. Rev. Lett.* 47 (1981) 1913.
[52] S. Nie, R.M. Feenstra, J.Y. Lee, M.H. Kang, *J. Vac. Sci. Technol. A* 22 (4) (2004) 1671.
[53] G. Bussetti, B. Bonanni, S. Cirilli, A. Violante, M. Russo, C. Goletti, P. Chiaradia, O. Pulci, M. Palummo, R.D. Sole, P. Gargiani, M.G. Betti, C. Mariani, R.M. Feenstra, G. Meyer, K.H. Rieder, *Phys. Rev. Lett.* 106 (2011) 067601.
[54] K. Löser, M. Wenderoth, T.K. Spaeth, J.K. Garleff, R.G. Ulbrich, M. Pötter, M. Rohlffing, *Phys. Rev. B* 86 (2012) 085303.
[55] C.H. Patterson, S. Banerjee, J.F. McGilp, *Phys. Rev. B* 84 (2011) 155314.
[56] F. Ancillotto, W. Andreoni, A. Selloni, R. Car, M. Parrinello, *Phys. Rev. Lett.* 65 (1990) 3148.
[57] M. Zitzlsperger, R. Honke, P. Pavone, U. Schroder, *Surf. Sci.* 108 (1997) 377.

- [58] D.E. Aspnes, J.F. Harbinson, A.A. Studna, L.T. Florez, J. Vac. Sci. Technol. A 6 (1988) 1327.
- [59] P. Weightman, D.S. Martin, R.J. Cole, T. Farrel, Rep. Prog. Phys. 68 (2005) 1251.
- [60] K. Lüdge, P. Vogt, O. Pulci, N. Esser, F. Bechstedt, W. Richter, Phys. Rev. B 62 (2000) 11046.
- [61] C. Violante, A.M. Conte, F. Bechstedt, O. Pulci, Phys. Rev. B 86, (2012) 245313.
- [62] M. Rohlfing, S.G. Louie, Phys. Rev. Lett. 83 (1999) 856.
- [63] C. Goletti, G. Bussetti, F. Arciprete, P. Chiaradia, G. Chiarotti, Phys. Rev. B 66 (2002) 153307.
- [64] C. Goletti, G. Bussetti, P. Chiaradia, G. Chiarotti, J. Phys. Condens. Matter 16 (2004) S4289.
- [65] H.A. Krassig, Cellulose, CRC Press, The Netherlands, 1993.
- [66] A.C. O'Sullivan, Cellulose 4 (1997) 173.
- [67] M. Missori, C. Mondelli, M.D. Spirito, C. Castellano, M. Bicchieri, R. Schweins, G. Arcovito, M. Papi, A.C. Castellano, Phys. Rev. Lett. 97 (2006) 238001.
- [68] M.D. Spirito, M. Missori, M. Papi, G. Maulucci, J. Teixeira, C. Castellano, G. Arcovito, Phys. Rev. E 77 (2008) 4 (Part 1).
- [69] S. Zervos, Natural and Accelerated Ageing of Cellulose and Paper: A Literature Review, Nova Publishing, New York, 2010.
- [70] M. Missori, M. Righini, S. Selci, Opt. Commun. 231 (2004) 99–106.
- [71] M. Missori, M. Righini, A.-L. Dupont, Opt. Commun. 263 (2) (2006) 289–294.
- [72] J. Lojewska, M. Missori, A. Lubanska, P. Grimaldi, K. Ziba, L.M. Proniewicz, A.C. Castellano, Appl. Phys. A 89 (2007) 883.
- [73] T. Lojewski, K. Zieba, A. Knapik, J. Bagniuk, A. Lubanska, J. Lojewska, Appl. Phys. A 100 (2010) 809.
- [74] T. Lojewski, P. Miskowiec, M. Missori, L.M.P.A. Lubanska, J. Lojewska, Carbohydr. Polym. 82 (2010) 370.
- [75] M. Strlic, J. Kolar, Aging and Stabilisation of Paper, National and University Library, Ljubljana, 2005.
- [76] A. Bos, J. Appl. Polym. Sci. 16 (1972) 2567.
- [77] A.M. Conte, O. Pulci, A. Knapik, J. Bagniuk, R.D. Sole, J. Lojewska, M. Missori, Phys. Rev. Lett. 108 (2012) 158301.
- [78] G. Kortum, Reflectance Spectroscopy (Principles, Methods, Applications), Springer-Verlag, Berlin/Heidelberg/New York, 1969.
- [79] B. Philips-Invernizzi, D. Dupont, C. Cazé, Opt. Eng. 40 (1964) 1082.
- [80] M.E. Casida, in: J.M. Seminario (Ed.), Recent Developments and Applications of Modern Density Functional Theory, Elsevier, Mont Réal, Québec, 1996.
- [81] A.M. Conte, O. Pulci, R.D. Sole, A. Knapik, J. Bagniuk, J. Lojewska, L. Teodonio, M. Missori, e-J. Surf. Sci. Nanotechnol. 10 (2012) 569.
- [82] A.Y. Matsuura, N. Thrupp, X. Gonze, Y. Pouillon, G. Bruant, G. Onida, Comput. Sci. Eng. 14 (2012).